CHAPTER 1

INTRODUCTION

Materials are probably more deep-rooted in human life than most of us realize. The earliest humans had access to only a few types of materials, those that occur naturally: stone, wood, clay, skins, and so on. With time mankind discovered techniques for producing materials that had properties superior to those of the natural ones. Likewise, it was discovered that the properties of a material could be altered since the scientists understand the relationships between the structural elements of materials and their properties. Thus, Different materials have evolved with rather specialized characteristics that meet the needs of human modern and complex society. During the last few decades, there has been an enormous interest in nanostructure materials due to their conspicuous physical-chemical properties. These properties originate from the fact that nanoscale materials with individual building blocks consisting of only 100-10,000 atoms have unique structures and behavior that cannot be extrapolated from our understanding of the bulk materials [1]. For example, the magnetic properties of nanoparticles of iron oxide are weaker than those of the bulk materials.

Several researchers have developed the methods of synthesis employed for the nanomaterials. The top-down methods rely on continuous breakup of bulk matter while on the other are the bottom-up methods that build up nanomaterials from their constituent atoms. The top-down and bottom-up approaches can also be considered as physical and chemical methods, respectively [2]. The top-down approach starts with a

bulk material and attempts to break it down into nanoscale-materials through physical methods. Hence, most of these techniques are really forms of fabrication rather than synthesis [3]. For the chemical approach (bottom-up), most nanomaterials are chemically synthesized in a solution phase and subsequently, compacted or assembled into macroscopic materials. Various chemical methods, such as hydrothermal and solvothermal routes [4-5], surfactant-assisted approach [6], have been utilized for the synthesis of nanostructured materials. Most physical and chemical properties of these nanomaterials are sensitively dependent on their size and shape, so the researchers are still focusing on developing simple and effective methods for the synthesis of nanomaterials of controlled size and morphology. Besides that, a variety of hybrid methods have since come into being such as microwave-assisted synthesis of materials. The utilization of microwave technology for the development of materials synthesis has been extensively studied since the last decade. The technology is generally applicable to synthesize in medicinal and combinatorial chemistry, and compared to conventional methods offers enhanced speed, reproducibility and scalability [7].

A number of researches have illustrated the continuing interests in new multinary chalcogenides materials [8]. The Cu-based multinary sulfides are of considerable interest because they exhibit novel structure and unusual physical properties. They have found applications as semiconductors, non-linear optical, superconductor, and photovoltaic cell materials. For example, $CuInS_2$ and $CuInSe_2$ have attracted considerable attention in recent years due to commercial thin film photovoltaic devices based on $Cu(In,Ga)(Se_2,S_2)$ but the element indium in natural reserves is relatively rare which limits these copper indium sulfide or selenide for

application in photovoltaic device. Therefore, development of new semiconductors instead of copper indium sulfides is imminently required [9].

1.1 Crystal structures and properties of ternary metal sulfide

1.1.1 Copper bismuth sulfide, Cu_3BiS_3, Wittichenite

The Cu_3BiS_3 is found as a naturally occurring bismuth sulfosalt of copper. Based on the mineral samples of this compound found in Wittichen mines, Baden, Germany, the compound has the mineralogical name Wittichenite [10]. In the mineral form, the structure of the compound has been determined as orthorhombic : a = 7.66 Å, b = 10.31 Å, c = 6.69 Å [10,11] with a measured mass density of 6.01 x 10^3 kg m^{-3} and a calculated mass density of 6.19 x 10^3 kg m^{-3} [12,13]. Nearly the same cell dimensions were confirmed later on a more detailed study in which the synthetic material was also prepared by heating a stoichiometric mixture of the elements [11, 12]. Its structure is orthorhombic, space group $P2_12_12_1$, (a = 0.7723 nm; b = 1.0395 nm; c = 0.6716 nm). The compound is stable at room temperature, and is among 13 compounds identified in the Bi–Cu–S ternary alloy system [14]. The density of the synthetic Cu_3BiS_3 was found to be 6.19 x 10^3 kg m^{-3}, the same as that calculated for the cell dimension with 4(Cu_3BiS_3) per cell.

E. Makovicky [15] studied phase transformations and thermal expansion of Cu_3BiS_3 up to 300 ^oC using heated Weissenberg and Guinier cameras. At 118.5 ^oC a transformation takes place from the $P2_12_12_1$ to a modulated $Pn2_1a$ or Pnma polymorph. The modulation changes continuously, with decreasing intensities of X-ray satellites. At 191 ^oC an unmodulated, high Pnma polymorph is formed. The lattice parameters are a = 7.705, b = 10.400, and c = 6.720 Å at room temperature. They

expand only slightly in the low form; a and c contract in the intermediate form, and c contracts further in the high form. The unit cell volume remains nearly constant between 25 and 300 ^{o}C. The observed phenomena result from redistributions of copper atoms over available structural sites and from the conversion of these atoms from a stationary to a mobile state.

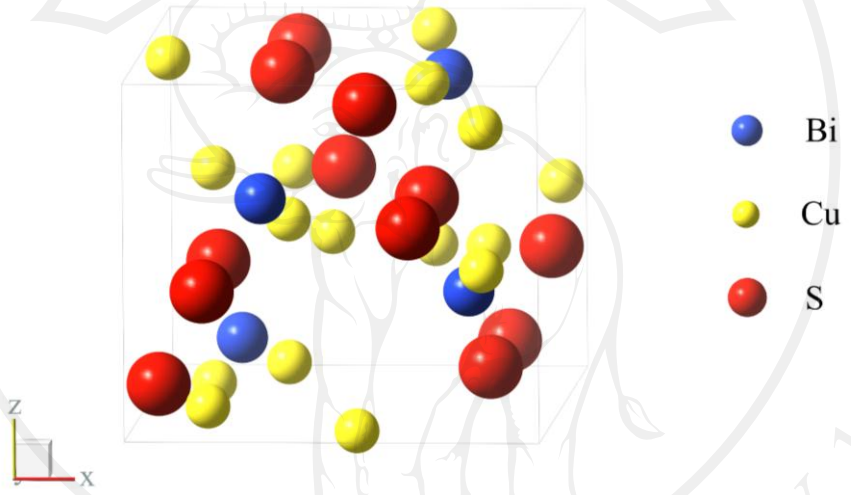

Figure 1.1 The crystal structure of Cu_3BiS_3 compounds [28]

P.K. Nair et al. [11] reported the formation of a ternary compound Cu_3BiS_3 by annealing process. The resulting film is optically absorbing in the visible region and exhibits p-type conductivity. In these Cu_3BiS_3 compound, a copper deficiency in the system leads to a p-type conductivity in the material. The characteristic results denoted the application of these films as solar control coating suitable for application in heterojunction solar cell structures. Other properties of Cu_3BiS_3 were investigated by F. Mesa group [16] by study of Cu_3BiS_3 thin films on soda-lime glass substrates prepared by co-evaporation of the precursors in a two-step process; The films were

characterized and results revealed that the Cu_3BiS_3 films present p-type conductivity, a high absorption coefficient (greater than 10^4 cm^{-1}), and an energy band gap, E_g, of about 1.39 eV. They found that carrier transport is thermally activated with activation energies fluctuating between 0.17 and 0.28 eV. This suggests that this compound has good properties to perform as absorbent layer in thin-film solar cells.

1.1.2 Copper antimony sulfide, Cu_3SbS_4, Famatinite

Cu_3SbS_4 is a compound in a family group IB-VA-VIA semiconductor which is obtained attention due to their important in solid-state chemistry and potential applications as small band-gap semiconductors [17]. In the past, there were extensively studied of electrical, thermal and thermoelectrical properties of Cu_3SbS_4 [17-19] together with the useful prediction about its non-linear optical properties [18]. Cu_3SbS_4 has been known in mineral name as Famatinite. It crystallizes in tetragonal with zincblende-related crystal structure, space group $I\bar{4}2m$. In mineral form, wet chemical and microprobe analyses showed the existence of solid-solution of famatinite(Cu_3SbS_4)-luzonite(Cu_3AsS_4) which have tetragonal, cubic-close packed structure. [20]. There are complete solid solution series between luzonite-famatinite [21] and neither luzonite nor famatinite have been found in absolutely pure masses [22]. Crystal structure of synthetic Cu_3SbS_4 was indicated by data from Single-crystal film techniques [23] which showed the tetragonal unit cell of compound with the refined parameters; a = 5.385 ± 0.001, c = 10.745 ± 0.002 Å and c/a = 1.997. Although, their structure is not cubic, there are no reports of anisotropic properties in these compounds [18].

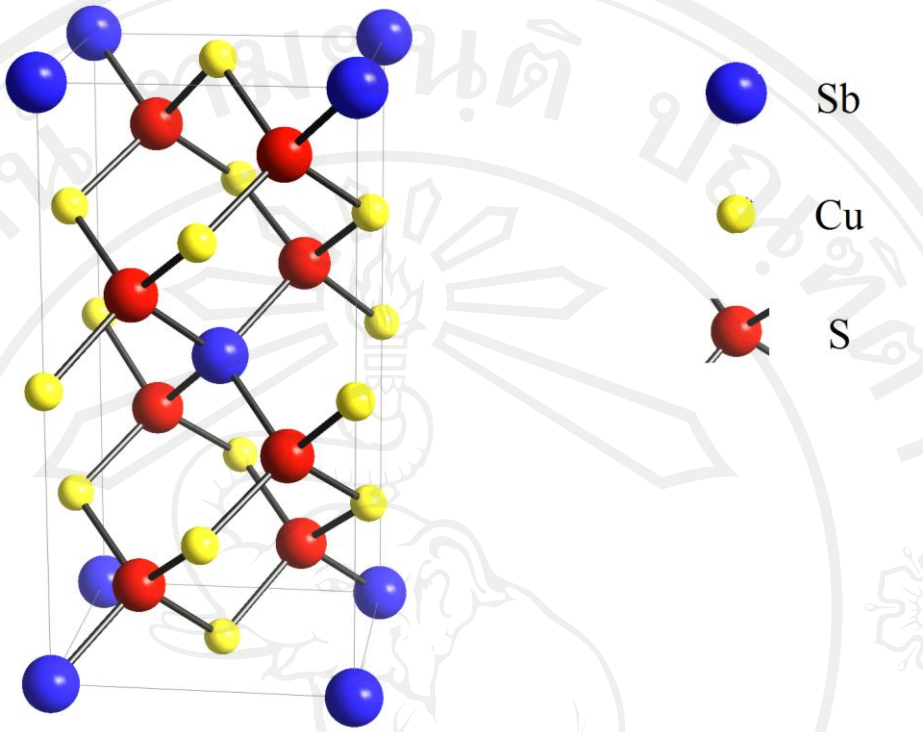

Figure 1.2 The crystal structure of Cu_3SbS_4 compounds [28-29]

E.J. Skoug et al. [19] have recently demonstrated that Cu_3SbSe_4 forms a complete solid solution with Cu_3SbS_4 resulting in a 40% reduction of its lattice thermal conductivity at room temperature. The Cu_3SbSe_4-Cu_3SbS_4 solid solution is promising for p-type thermoelectric applications because the electronegativity difference between Se^{2-} and S^{2-} is quite small which helps to conserve the carrier mobility in mixed-crystal semiconductors. In addition, the Se/S mixture should generate phonon-impurity scattering.

1.1.3 Copper iron sulfide, $CuFeS_2$, Chalcopyrite

$CuFeS_2$ is such a kind of semiconducting materials with a very small band gap of 0.5-0.6 eV [24]. It is well know as a natural mineral, which is exploited for Cu extraction in mines, but the pure chalcopyrite is rare in nature [25]. The crystal structure of $CuFeS_2$ can be considerable as a double sphalerite cell; an ordered arrangement of Cu and Fe ions is in tetrahedral coordination with S in the lattice. The bulk $CuFeS_2$ material has very unique magnetic, electrical and optical properties. The $CuFeS_2$ presents a tetragonal structure, with space group $I\bar{4}2d$ and lattice constant a = 5.289 Å and c = 10.423 Å (JCPDS 71-0507).

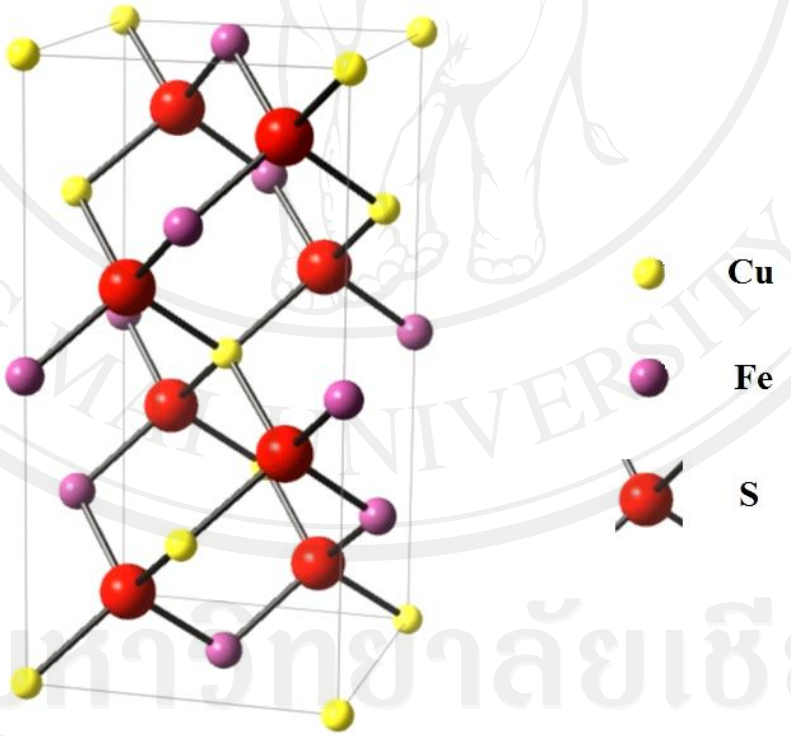

Figure 1.3 The crystal structure of $CuFeS_2$ compounds [28-29]

M.X. Wang et al. studied magnetic behavior of $CuFeS_2$ nanowire by Mössbauer spectroscopy. The Mössbauer spectrum consists of a six peak hyperfine magnetic spectrum (isomer shift, 0.3012 mms^{-1}; quadrupole splitting, -0.0358 mms^{-1}; internal magnetic field, 345.49 kilogauss), and interpret the presence of high-spin Fe^{3+} on the tetrahedral lattice sites of chalcopyrite structure. From the values of the isomer shift, it is evident that the compound is practically composed of $Cu^{+}Fe^{3+}S_2^{2-}$ charged atoms [26]. S.D. Disale and S.S. Garje also investigated the magnetic property of $CuFeS_2$ nanoparticles prepared by pyrolysis route. It was found to exhibit magnetic properties at room temperature with saturation magnetization of 16-19 emu g^{-1} [27].

1.2 Application of ternary metal sulfide

H. Hu et al. [30] presented a technique for preparing electrically conductive coatings of Cu_3BiS_3 powder in polyacrylic acid (PAA) matrix. Bi_2S_3 powder was introduced into a freshly prepared CuS. The as-obtained CuS–Bi_2S_3 powder was mixed with PAA aqueous solution, and the resulting mixture was used as a paste to form a screen-printed composite coating. The polymer acts as a matrix in which the precipitate is embedded, and at the same time the coating is attached to the substrate by the same PAA. The presence of PAA does not affect the thermal stability of the coatings' electrical properties or their phase transition process. Electrical sheet resistance of the coatings is analyzed as a function of the Bi_2S_3:CuS ratio, as well as annealing temperature and atmosphere.

F. Mesa et al. [31] analyzed the type of doping, free carrier concentration, thermoelectric power, surface work function, and defect states in the band gap. They formed a heterojunction of Cu_3BiS_3 with In_2S_3 in order to demonstrate efficient

surface defect passivation of Cu_3BiS_3 and investigate the band bending of the Cu_3BiS_3 / In_2S_3 structure. Samples were prepared by coevaporation onto a substrate at 300 °C in a chamber with a base pressure of 10^{-5} mbar. Deposition of In_2S_3 was performed by coevaporation of Indium (In) and Sulfur (S) inside the same vacuum chamber, immediately after the Cu_3BiS_3 deposition.

Y. Zeng et al. [32] reported the flower-like Cu_3BiS_3 hierarchical nanostructures synthesized by a simple solvothermal route. These Cu_3BiS_3 hierarchical nanostructures with an outer diameter about 8 μm were confirmed to be mesoporous. The optical band gap of the as-prepared Cu_3BiS_3 nanostructures is also examined to be 1.2 eV. They investigated the electrochemical properties of these nanostructures as anode materials for the lithium-ion battery. Electrochemical measurements showed that the initial discharge capacity of the nanosheet based Cu_3BiS_3 hierarchical structures is 676 mA h g^{-1} which is larger than the theoretical value of Bi_2S_3 (625 mA h g^{-1}), but it degraded quickly during subsequent cycles, and further improvement in cyclic stability is still needed for practical application in lithium-ion batteries.

J. Yan et al. [33] studied the procedure for the polymerization of octadecylsilane ($C_{18}H_{37}SiH_3$) by using Cu_3BiS_3 as catalysts for polymerization. They found that Hypocrellins, PVP (polyvinyl pyrrolidone) and PEG (polyethylene glycol) templates had strong effects on the morphologies of synthesized Cu_3BiS_3 and their catalytic polymerization products of an octadecylsilane ($C_{18}H_{37}SiH_3$). The polymerization product resulted from the materials templated by hypocrellins shows good replica of the morphologies before polymerization while significant morphology

change during polymerization was observed when the materials template by PVP and PEG templates was used as catalysts for the polymerizations.

Cu_3BiS_3 is also suitable for many applications due to the minimizing concerns about material availability and toxicity. Bismuth is currently used in pharmaceuticals and as a replacement for lead in ammunition, solders, and other materials where toxicity is a concern and bismuth is readily available, and the use of bismuth-containing compounds in place of CIGS or CdTe would raise the energy production ceiling of thin film photovoltaic technologies [34]. Moreover, Cu_3BiS_3 is one of the promising materials for low cost thin film solar cells technology because of its optimum energy band gap (E_g) and a high fundamental absorption coefficient. Cu, Bi and S are abundant in nature and they do not contribute to pollution during the Cu_3BiS_3 growing process [35].

$CuFeS_2$ material was applied in Li/CuO battery as an additive [36]. The discharge characteristics of the Li/CuO system have been improved by adding chalcopyrite ($CuFeS_x$, $1.6 < x \leq 2$) to the cathode. The open-circuit voltage of synthetic chalcopyrite was ~ 0.2 V lowers than that of cupric oxide. Chalcopyrite shows no voltage depression when discharged and only causes a relatively small increase in the cell thickness on its discharge. Both chalcopyrite and cupric oxide have a low solubility in the organic electrolyte. A cathode system composed of cupric oxide and chalcopyrite has the following properties: a brief excursion to the plateau voltage, no voltage depression at the beginning of discharge, only a small increase in the cell thickness, and a good storage life. Button cells using this system have been successfully developed for electronic devices.

1.3 Literature reviews

1.3.1 Synthesis of copper bismuth sulfide, Cu_3BiS_3

1.3.1.1 Solid-state reactions

Over the past decades, there have been a number of synthetic methods for preparation of Cu_3BiS_3 thin film and also powder. For instance, N. J. Gerein and J. A. Haber [37] have used a one-step process by reactive sputter deposition to synthesized Cu_3BiS_3 thin films on fused silica hot substrates. Films were deposited by sputter deposition from CuS and Bi and the sputtering gas was Ar. To deposit compound films on hot substrates with the desired 3:1:3 stoichiometry, they sputtered the CuS target continuously and cycled the Bi target on and off. This one-step process produces films that are crystalline, phase-pure, dense, smooth, and continuous. Post-deposition annealing in an H_2S atmosphere increases crystallite size and reduces electrical resistivity of films. Moreover, they investigated the synthesis of Cu_3BiS_3 thin films on fused silica substrates by heating Cu-Bi metal precursor films and Cu-S-Bi metal sulfide precursor films, sputter in a H_2S atmosphere. Phase-pure Cu_3BiS_3 films 250-1000 nm thick were formed. It was found that precursor composition determines the reaction pathway, and is the dominant factor in controlling the morphology of Cu_3BiS_3 thin film.

Thin films of Cu_3BiS_3 have been produced by conversion of stacked and co-electroplated Bi–Cu metal precursors in the presence of elemental sulfur vapor by D. Colombara group [38]. The roles of sulfurization temperature and heating rate in achieving single-phase good quality layers have been explored. The potential loss of Bi during the treatments has been investigated, and no appreciable compositional difference was found between films sulfurized at 550 °C for up to 16 h. The

structural, morphological and photoelectrochemical properties of the layers were investigated in order to evaluate the potentials of the compound for application in thin film photovoltaics.

1.3.1.2 Hydrothermal/Solvothermal synthesis

In recent years, many researchers have focused intently on hydrothermal or solvothermal synthesis of Cu_3BiS_3. J.Hu et al. [39] prepared nanocrystalline Cu_3BiS_3 at low synthetic temperature by convenient hydrothermal process. The autoclave was maintained under auto-generated pressure at temperature range of 100–150 ^oC for 10 hours. The as-prepared Cu_3BiS_3 sample consisted of whisker-like particles. Preliminary results showed that the prepared precursors, reaction temperature and time played a role in the formation of the final products.

After that, D. Chen et al. [40] also reported that Cu_3BiS_3 nanorods with different aspect ratios have been synthesized via an ethanol thermal pathway using different solvents. The autoclave was filled with ethanol, or ethylene glycol, or glycerine up to 80% of the total volume and maintained at 160 ^oC for 10 hour. The Study found that the key factor which influences the aspect ratio of as-prepared Cu_3BiS_3 nanorods is solvent. The possible reaction mechanism may involve the formation of metal–thiourea complexes and thermal decomposition.

Flower-like Cu_3BiS_3 nanorods were synthesized by J. Zhong et al. [41] via a facile biomolecule-assisted solvothermal method at 200 °C for 16 h, employing $CuCl_2{\cdot}_2H_2O$, $Bi(NO)_3{\cdot}5H_2O$ and L-cysteine as reactants. The morphology, structure, and composition of the obtained products were studied. Results indicated that the flower-like Cu_3BiS_3 nanostructure consists of many nanorods with an average diameter about 150 nm. Moreover, the optical properties of flower-like Cu_3BiS_3

nanorods were investigated by Raman and photoluminescence spectroscopy. The PL spectrum showed that a strong UV emission peak located at around 356 nm and a weak and shoulder emission situated at 379 nm. Raman spectrum exhibited four distinct vibrational peaks at about 116, 153, 355 and 459 cm^{-1}.

1.3.1.3 Single-source precursors

G. Shen et al. [42] prepared coral-shaped Cu_3BiS_3 nanostructures at low temperature via a polyol process. By refluxing the single-source precursors, metal diethyldithiocarbamate, in ethylene glycol. In a typical procedure, a stoichiometric mixture of $Bi(S_2CNEt_2)_3$ and $Cu(S_2CNEt_2)_2$, isolated readily from an alcohol solution of metal ions and sodium diethyldithiocarbamate, was placed into a three-necked, round bottom flask of 250 ml capacity that was filled with 50 ml ethylene glycol. The flask was heated and maintained at 195 ^oC for 1 h under magnetic stirring and then cooled to room temperature. The final black powders were obtained.

1.3.2 Synthesis of copper antimony sulfide, Cu_3SbS_4

1.3.2.1 Hydrothermal/Solvothermal synthesis

C. An et al. [17] designed a low temperature solution synthesis route, which conveniently produces high quality Cu_3SbS_4 nanofibers on a large scale. The process has no participation of catalysts or templates and requiring no expensive precision equipment. CuCl, $SbCl_3$ and NH_2CSNH_2 were used as raw materials in this method. Distilled water and absolute alcohol were selected as the reaction media. It was found that the reaction media and reaction temperature play important roles in controlling the phases and morphologies of the final products. The high product yields and low

reaction temperature employed mean that this simple method has good prospects for use in related future applications.

1.3.2.2 Polyol-method

S. Bl¨oß and M. Jansen [43] synthesized Cu_3SbS_4 from metal chlorides and thiourea in form of microscale particles via an adjusted polyol route. Their work shows, that the adjusted polyol-method has a high potential for establishing a new synthesis route also to multinary sulphides. Famatinite (Cu_3SbS_4), have been synthesize by mixing 2.5 mmol of $CuCl_2$ and 2.5 mmol of $SbCl_3$, respectively, with an excess of thiourea (5 mmol) in 50 ml of diethylene glycol (DEG). The mixtures were heated for 1 or 5 h at 175 ◦C. In order to prevent the formation of the binary phase Covelite (CuS), one has to use an excess of antimony.

1.3.3 Synthesis of copper iron sulfide, $CuFeS_2$

1.3.3.1 Solid-state reaction

The chalcopyrite $CuFeS_2$ films have been grown in thin film form by sulphurization (20 min at 723 K) of CuFe alloy precursor [44]. Cu/Fe…/Cu thin layers have been sequentially deposited by vacuum evaporation on a substrate heated at 723 K. After deposition of the metal alloy precursor, there is an inter-diffusion of the metals all along the thickness. It has been shown that the films achieved present interesting structural and optical properties. The optical absorption measurements revealed that the band gap energy obtained in this work is $E_g = 0.575$ eV.

$CuFeS_2$ was also synthesized by direct reaction of a stoichiometric mixture of the pure elements (Fe, Cu and S, 99.95%) in a fused silica tube evacuated to $< 10^{-4}$ torr and sealed. The sealed tube was placed in a furnace and heated at 723 K for 7

days, prior to cooling at the natural rate of the furnace. The sample was then reground to homogenize it, prior to re-firing at 1173 K for 2 days. The sample was finally cooled to room temperature at 25 Kh^{-1}[45].

1.3.3.2 Hydrothermal /Solvothermal synthesis

$CuFeS_2$ nanoparticles were synthesized using a hydrothermal chelation method at relatively low temperature and without introducing organic solvents [46]. The citric acid was added as a chelating agent, which may decrease the impurity phase. The characterization results showed that the citric acid could form chelating complexes with iron and copper and promote the hydrothermal reaction. The citric acid significantly affected the purity of the obtained powders presumably due to its formation of complexes with copper and iron, thus increasing the probability of sulfur-based anionic group reaction with copper and iron ions at the same time. The synthesized $CuFeS_2$ nanoparticles have cuboidal crystal forms with particle sizes between 100 and 200 nm. The energy gap was measured to be 0.53 eV.

A solventothermal reaction route has been developed by M.X.Wang group to prepare chalcopyrite phase $CuFeS_2$ based on the reactions between CuCl, $FeCl_3$ and $(NH_4)_2S$ in ethylenediamine [47]. The nanowires with a diameter of about 50 nm and a length up to several micrometers were prepared at 150–220 ^oC. The SEM and the TEM images show the $CuFeS_2$ single crystal nanowires with a diameter of about 50 nm and a length up to several micrometers. The magnetic behavior of iron in chalcopyrite $CuFeS_2$ was studied. Ethylenediamine played an important role in the formation of the ternary sulfides. At the proper temperature and time, the reactions could steadily proceed, the nucleation and the growth were easily controlled, and the nanocrystalline $CuFeS_2$ formed homogeneously. The mechanism is proposed to

explain the chemical reactions, and the influence of various factors on the formation of the $CuFeS_2$ nanowires was discussed.

1.3.3.3 Single source precursor

Nanocrystalline chalcopyrite ($CuFeS_2$) have been synthesized using single-source precursors, CuL_2 and $Cu(LH)_2Cl_2$ (where LH = monoacetylferrocene thiosemicarbazone) by pyrolysis and solvothermal decomposition methods [27]. The $CuFeS_2$ crystallites obtained by pyrolysis of CuL_2 and $Cu(LH)_2Cl_2$ have a cubic phase and rod-like morphology with diameters of about 18 and 15 nm, respectively, and lengths of about 195–390 and 100–145 nm, respectively. On the other hand the $CuFeS_2$ crystallites prepared by solvothermal from CuL_2 and $Cu(LH)_2Cl_2$ were found to be capped with ethylene glycol and they possessed spherical shape with an average grain size of 16 and 11 nm, respectively. The experimental conditions such as decomposition temperature and refluxing time affect the properties like crystallinity, morphology and magnetic properties of the $CuFeS_2$.

1.4 Microwave radiation synthesis

1.4.1 A Brief history of microwave radiation synthesis

Recently, heating and accelerating chemical reactions by microwave energy have been increasingly popular attentions in the scientific researches. Microwave energy has found a variety of applications in chemical and related industries since 1950s, in particular in the food-processing, drying, and polymer industries [48]. The first academic reports on the use of microwave heating to mediate organic chemical reactions were published by the groups of Gedye [49] and Giguere [50] in 1986. These early experiments of microwave-assisted organic synthesis (MAOS) were

typically carried out in sealed Teflon or glass vessels in a domestic household microwave oven without any temperature or pressure measurements. Although there were several violent explosions due to the rapid uncontrolled heating of organic solvents in those early days, an increasing number of scientists started to investigate this new approach.

Microwave-assisted synthesis in solution also has been carried out under open vessel conditions. However, if solvents are heated by microwave irradiation at atmospheric pressure in an open vessel, the boiling point of the solvent limits the reaction temperature. The microwave-absorbing solvents with high boiling points have been frequently used in open-vessel microwave synthesis (e.g. DMF, NMP, ethylene glycol) in order to achieve high reaction rates. Due to the beneficial of rapid heating by microwaves irradiation, this approach might be the forthcoming method of choice for materials synthesis on a laboratory scale. Furthermore, recent innovations in microwave reactor technology allow controlled and automated sequential processing under sealed vessel conditions, and the use of continuous flow (CF) reactors or stop-flow (SF) reactors for scale-up purposes. When closed-vessels are used the microwave heating helps increase the pressure inside the vessel. This process allows an increase of the boiling point of the reagents, which has important kinetic and thermodynamic implications [51].

For instance synthesis of inorganic materials, T. Thongtem et al. have been synthesized nanostructured $AgBiS_2$ with the shape of flowers and hexapods using cyclic microwave-assisted synthesis. Microwave radiation could be used for the synthesis of nanostructured materials since it can solve the problems of temperature and concentration gradients, and provides uniform growth media [52]. By

understanding with proper control, many important materials can be heated rapidly, uniformly, selectively, less expensively and with greater control than is by using conventional methods. Moreover, the microwave energy distribute to the unique internal heating phenomenon can lead to products and processes that cannot be achieved by conventional methods [53].

1.4.2 Microwave radiation

Electromagnetic (EM) radiation is a form of energy radiated in the form of a wave traveling at the speed of light, comprising both electric and magnetic fields that oscillate at right angles to each other and in the direction of propagation. In the electromagnetic spectrum, microwave radiation occurs in an area of transition between infrared radiation and radiofrequency wave which lies in the range of frequencies between 300 MHz to 300 GHz and wavelengths of 1 m to 1 mm respectively (figure 1.4). Due to their rapid development during World War II, microwaves have been expanded to numerous applications especially in radar and communication. The various applications of microwaves are in microwave heating, navigation, electronic warfare, medical equipment for radiology treatment, scientific and industrial instruments, etc.

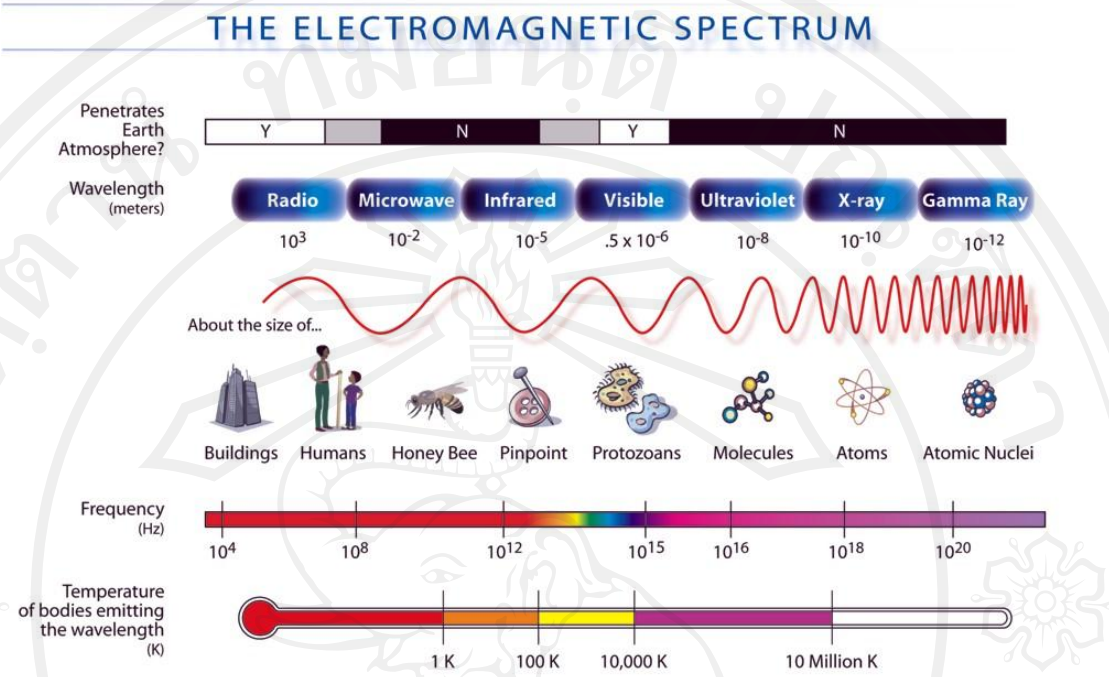

Figure 1.4 The range of wavelengths and frequencies of electromagnetic spectrum (image courtesy of NASA).

Although microwave frequencies range from 300 MHz to 300 GHz, most of the frequencies are restricted to government usage and only a limited range of frequencies available for commercial and domestic usage in order to avoid the interference with telecommunication and cellular phone frequency. For microwave heating, two frequencies, reserved by the Federal Communications Commission (FCC) for industrial, scientific, and medical (ISM) purposes are authorized to operate only at either 915 MHz or 2.45 GHz. However, microwave heating and most commercial microwave ovens generally operate at a frequency of 2.45 GHz [54-55]. Microwaves can be further classified into three bands: the Ultra High Frequency (UHF) band with frequencies ranging from 300 MHz to 3 GHz, the Super High

Frequency (SHF) band with frequencies ranging from 3 to 30 GHz and the Extremely High Frequency (EHF) band with frequencies ranging from 30 to 300 GHz [53].

The considering of Maxwell's electromagnetic theory is essential for the understanding of microwave. The electromagnetic theory proposed by Maxwell provided a mathematical structure for understanding the combined effects of electricity and magnetism. The propagation and excitation in electromagnetic waves are dominated by Maxwell's equations. By applying appropriate boundary conditions to the equation, analysis of the interaction of microwave with materials can be performed. The Maxwell's equation is shown below;

$$\nabla x\, E = \frac{\partial B}{\partial t} \quad , \quad \nabla \bullet B = 0$$

$$\nabla x\, H = \frac{\partial D}{\partial t} + I \quad , \quad \nabla \bullet D = \rho,$$

Where E is the electric field vector, H, is the magnetic field vector, D is the electric flux density vector, B is the magnetic flux density vector, I is the current density vector, and ρ is charge density. The Maxwell equations are the physical laws that describe electromagnetic fields that vary with time. Eventually, analysis of Maxwell's equation in more details can be found in electromagnetic theory textbooks.

1.4.3 Microwave-material interactions [53, 54, 57]

Many researchers have been made efforts to explain the mechanisms of microwave-material interactions. Some groups of researchers used molecular orbital model to predict the behavior of species in a microwave field [56]. Another group explained base on the physics of interaction and dielectric properties of materials [53]. In this research, the physics of interaction and dielectric properties of materials are

mentioned and discussed. Generally, the electric field component of the electromagnetic wave may be reflected, transmitted or absorbed by materials and magnetic materials can interact with the magnetic field component of the electromagnetic wave. The interaction of microwaves with materials can be classified by different sort of materials into the following categories;

1) Opaque materials

This refer to conducting materials with free electrons (typically metals) which is reflect and do not allow electromagnetic waves to pass through.

2) Transparent materials:

These are low dielectric-loss materials (insulating materials such as glass, ceramics and air) which reflect and little absorb electromagnetic waves and allow microwaves to pass through easily with little attenuation.

3) Absorbing materials

Mostly are high dielectric-loss materials (materials with properties range from conductors to insulators) which absorb electromagnetic energy and convert it to heat.

4) Magnetic materials

Materials will interact with the magnetic component of the electromagnetic wave and get heated.

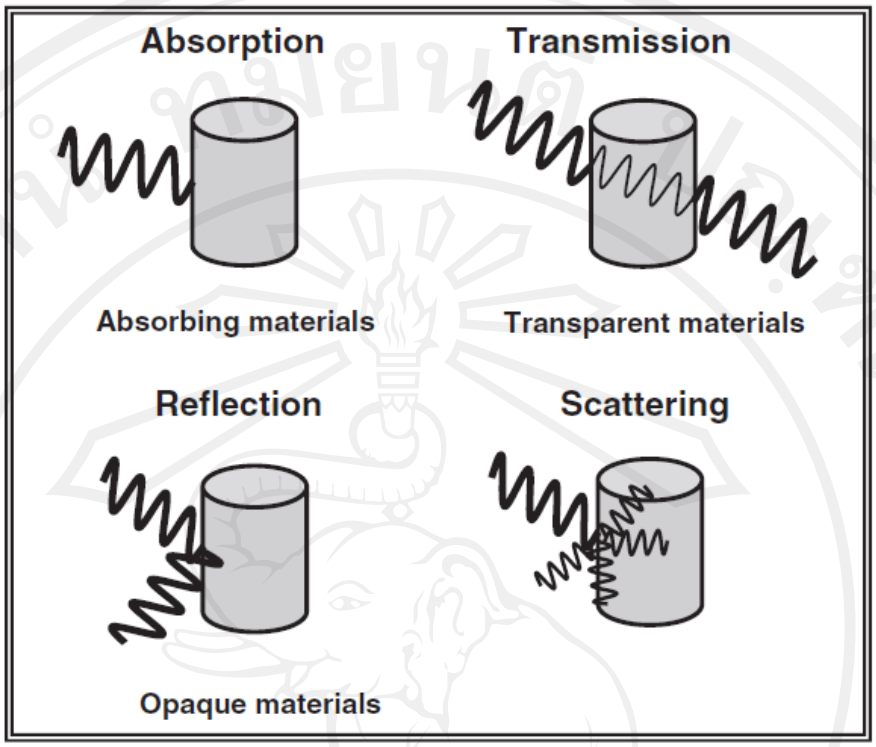

Figure 1.5 Interaction of the electromagnetic field with materials [after Ref. 53]

By considering the physics of interaction in microwave heating of materials, the interaction between electromagnetic waves and materials is quantified by two complex physical quantities, the dielectric permittivity, ε' and the magnetic permeability, μ'.

Permittivity, ε', also know as the dielectric constant, describes the response of a dielectric material to an applied electric field. Dielectric response of materials may cause by a number of properties. These properties include electronic polarization, atomic polarization, orientation (dipolar) polarization, and Maxwell-Wagner polarization mechanisms. At microwave frequencies, dipolar polarization is thought to be the most important mechanisms for energy transfer at the molecular level. In

composite materials, Maxwell-Wanger polarization is also an important heating mechanism.

The absolute permittivity (or dielectric constant) is the product of permittivity of free space (ε_o = 8:854 x10^{-12} F/m) and relative permittivity, $\varepsilon_r^{'}$.

$$\varepsilon^{'} = \varepsilon_o \varepsilon_r^{'}$$

The complex permittivity is a measure of the ability of a dielectric to absorb and store electrical potential energy, with the permittivity, $\varepsilon^{'}$, representing the penetration of microwaves into the material and the dielectric loss factor, $\varepsilon^{"}$, representing the ability of the material to store energy. The complex permittivity, ε^{*}, is formally introduced as Equation below.

$$\varepsilon^{*} = \varepsilon^{'} - j\varepsilon^{"}$$

The loss tangent, tan δ, represents the efficiency of the material to convert absorbed energy into heat and is also used commonly to describe the dielectric response.

$$\tan\delta = \frac{\varepsilon^{"}}{\varepsilon^{'}}$$

The angle δ is the phase difference between the oscillating electric field and the polarization of the material.

Permeability, μ', describes the response of a material to a magnetic field. The magnetic permeability is the product of permeability of free space ($\mu_o = 4\pi$ x 10^{-7} H/m) and relative permeability, $\mu_r^{'}$

Similar to the case on the use of complex permittivity to account for the losses of a material due to an alternating electric field, the complex permeability, μ^*, can be expressed by Equation below

$$\mu^* = \mu' - j\mu''$$

where μ'' represents the magnetic loss factor due to relaxation and resonance processes under the influence of an alternating magnetic field.

Permeability controls the penetration depth: the higher the permeability, the less an electromagnetic wave will penetrate into the material.

In microwave processing of materials, the interaction between the electric and magnetic field components of the microwaves and the materials can result in dielectric and magnetic losses, leading to heating. Dielectric losses have been studied extensively and can be attributed to the redistribution of charges or polarization under the influence of an alternating external electric field. In the heating of dielectric materials, it is assumed that the magnetic field does not contribute to microwave absorption and heating occurs entirely due to the electric field. However, there are no single theory can explain the response of materials with microwave because some high conductivity materials such as metal, the heating depends on conduction losses. In magnetic materials, magnetic losses such as hysteresis, eddy currents, domain wall and electron spin resonance contribute to the heating.

Polarization phenomena are expressed by the polarization, $\vec{P}$, which denotes the contribution by matter compared with that of vacuum. The electric field and the polarization are linked by Maxwell's equations. The constitutive equation for vacuum is given by;

$$\vec{D} = \varepsilon_0 \vec{E}$$

where $\vec{D}$ is the electric displacement and $\vec{E}$ is the electric field. For a dielectric medium characterized by ε_0 as in Equation;

$$\vec{D} = \varepsilon^* \vec{E} = \varepsilon_0 \vec{E} + \vec{P}$$

As in equation, the higher the dielectric permittivity of a material, the greater of the polarization processes. Depending on the frequency, the electromagnetic field can put one or more types of charge association under oscillation. In any material there is a variety of types of charge association.

For example:

- Inner electron tightly bound to the nuclei
- Valence electrons
- Free or conduction electrons
- Bound ions in crystal,
- Free ions in electrolytes and nonstoichiometric ionic crystal

For electron of the inner atomic shells the critical frequency is of the order of the X-ray and electromagnetic field of wavelength more than 10^{-10} nm which induces ionization of these atoms and there is no polarization effect on the material. In optical range electromagnetic field can induce distortion of inner and valence electronic shell, known as electronic polarization process. In infrared range electromagnetic field can induce atomic vibrations in molecules and crystal and polarization process result from the atomic polarization process. In microwave band, electromagnetic field leads to rotation of polar molecules or charge redistribution. The corresponding polarization process is denoted orientation polarization.

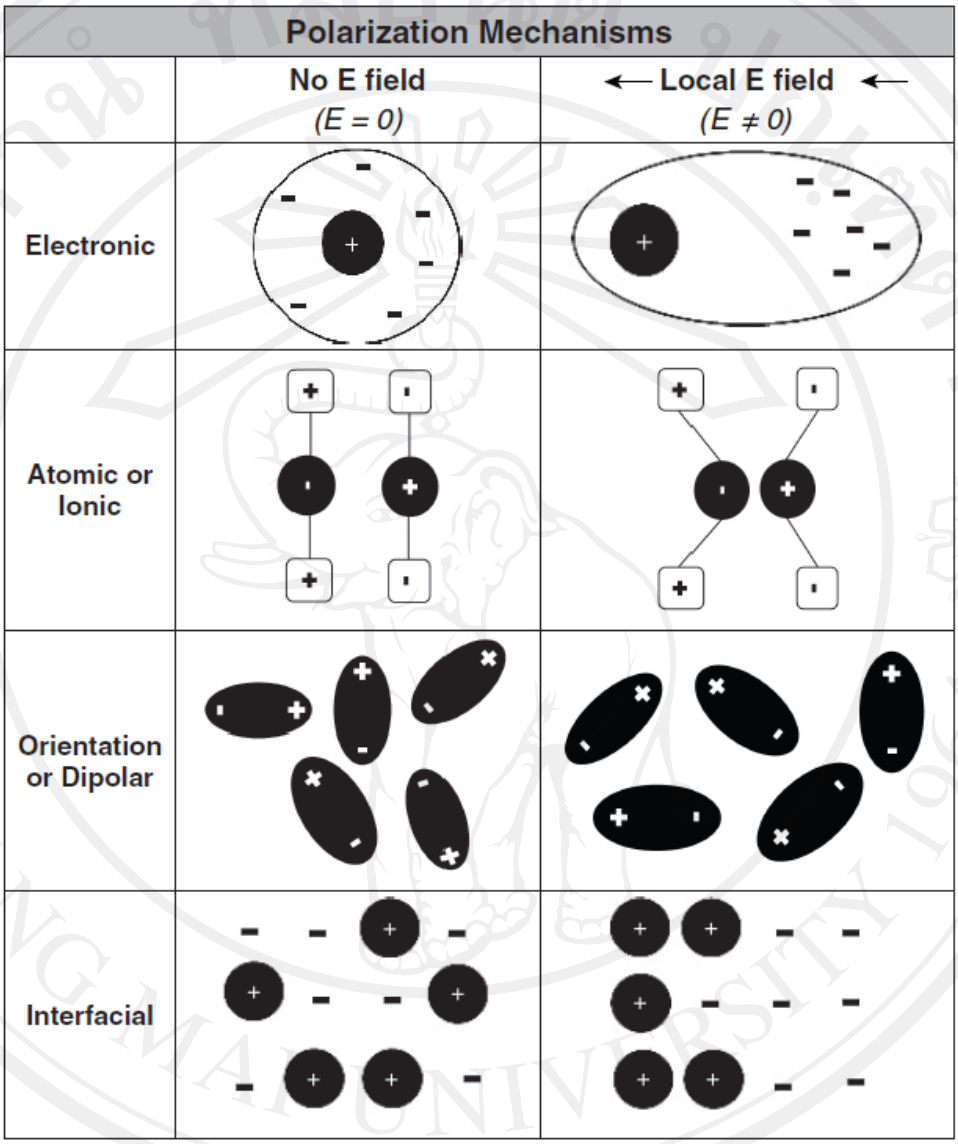

Figure 1.6 The various polarization mechanisms (after Ref. 53)

As shown in Figure 1.6, electronic polarization results from a dipole moment induced by distortion of electron shells. the net charge surround the atom is zero and there is no dipole moment in the absence of electric field, E. When the atom is subjected to an external electric field, the charges will be redistributed and the

electrons are shifted from equilibrium with respect to the positive nuclei, resulting in an induced dipole moment.

In atomic polarization occurs due to the relative displacements of the positive and negative ions or atoms within molecules and crystal structures from their equilibrium lattice sites, unlike electronic polarization where only displacement of the electron charges surrounding the nuclei occurs. In the neutral state, the positively and negatively charged ions in the crystal lattice are equally balanced and the net dipole moment is zero. Under an applied electric field, the positively and negatively charged ions in the crystals are displaced from their equilibrium positions so that the net dipole moment is no longer zero.

For orientation or dipolar polarization, result from some materials which are made up of molecules that contain permanent dipole moments. Normally, the molecules are randomly oriented in the material due to thermal activation and there is no net dipole moment. When an external electric field is applied, dipolar polarization occurs as the external electric field tries to align these asymmetric (polar) molecules having permanent dipoles parallel to the field. Under microwave frequencies, the dipoles respond to the external electric field by rotating to align with the field; however, a phase difference exists between the orientation of the field and that of the dipole, since the dipoles do not have sufficient time to respond to the rapidly fluctuating field. This phase difference causes energy to be released from the molecules upon random collision with other molecules, leading to dielectric heating.

Interfacial polarization, also termed Maxwell–Wagner or space charge polarization, involves the accumulation of free charges at interfaces located within the material or between differences. The material has an equal number of positive and

negative ions, therefore there is no separation of charges between the opposing ions in the absence of an electric field. When an external field is applied, the more mobile charges are displaced and accumulate at barriers such as grain/phase boundaries or at free surfaces, resulting in interfacial polarization.

1.4.4 Microwave heating [53-54]

Since, microwave heating originated from radio frequency heating and industrial applications started after World War II and the first commercial microwave oven, Radarange, was introduced in 1947 by Raytheon. Microwave heating has been applied to a wide variety of materials, including ceramics, polymers, metals, semiconductors, rubber, glass, minerals, biomaterials, chemicals, powders and wastes. Applications include drying, sintering, melting, brazing, joining, infiltration, diffusion, plasma processing, waste remediation and recycling. Moreover, the microwave synthesis is also favorite one of applications of the microwave heating. Microwave heating is based upon the ability of a material to absorb electromagnetic energy directly and to be heated. The heating effect has been attributed to the interaction of the electric field with material, while the magnetic field is usually ignored. Heating arises due to the ability of the electric field to polarize the charges in the material and the inability of the polarization to keep up with the rapidly changing electric field. Microwave heating possesses several unique characteristics that are different from conventional heating.

The main characteristics of microwave heating include: penetrating radiation; rapid heating; and selective heating of materials. In conventional heating, energy is transferred to the material through convection, conduction, and radiation of heat from

the surfaces of material to interior of material and energy is transferred to materials due to thermal gradients known as “heat transfer”. In contrast of microwave heating, energy is transferred to materials by interaction of the electromagnetic fields at the molecular level. Microwave heating is the transfer of electromagnetic energy to thermal energy and is energy conversion, rather than heat transfer. In addition microwaves can penetrate materials and deposit energy; heat can be generated throughout the volume of the material, resulting in volumetric heating. Hence, it is possible to achieve rapid and uniform heating of thick materials.

Penetration depth, d, or skin depth is a measure of the depth of microwave penetration in a material. The penetration depth of the field is defined as the distance from the surface of the material at which the magnitude of the field strength reduces to 1/e (=0.368) of its value at the surface. The penetration depth of the electric field can be expressed by the equation

$$d = 1/\alpha$$

where α is the attenuation factor and can be represented as

$$\alpha = 2\pi\nu\left(\frac{\mu_0\mu'\varepsilon_0\varepsilon'}{2}\right)^{1/2}[(1+(\tan\delta)^2)^{1/2}-1]^{1/2}$$

equation above shows that the penetration depth is inversely proportional to the frequency ν of the electromagnetic field.

The power penetration depth, D_p, can be defined as the distance at which the power density reduces to 1/e of its value at the surface and is half the value of the electric field penetration depth, d.

$$D_p = \frac{1}{2\alpha} = \frac{d}{2}$$

When electric field of microwave is in contact with materials having different dielectric properties, it will selectively couple with the higher loss tangent material. In multiple phase materials, some phases may couple more readily with microwave. It may be possible to process materials with new or unique microstructures by selectively heating distinct phases. Therefore, microwaves can be used for the selective heating of the materials. This difference in the way energy delivery can result in many potential advantages to use microwaves for processing or heating materials.

Microwave heating involves the conversion of electromagnetic energy to heat by the material. The power dissipated into or absorbed by the material by the conversion of electromagnetic energy into heat can be expressed by equations below;

Due to electric losses only; Average power (P_{av}) $= 2\pi\nu\varepsilon_0\varepsilon''_{eff}E^2_{rms}$

$= 2\pi\nu\varepsilon'(\tan\delta)E^2_{rms}$

ε''_{eff} refer to the effective relative dielectric loss factor

E^2_{rms} refer to the root mean square of the electric field

The effective relative dielectric loss factor is the summation of losses from polarization and conduction.

$$\varepsilon''_{\text{eff}} = \varepsilon''_{\text{polarization}} + \varepsilon''_{\text{conduction}}$$

$$\varepsilon''_{\text{eff}} = \varepsilon''_{\text{electronic}} + \varepsilon''_{\text{dipolar}} + \varepsilon''_{\text{atomic}} + \varepsilon''_{\text{interfacial}} + \sigma/\omega\varepsilon_0$$

σ = Dielectric conductivity

ω = Angular frequency

Numerous studies have reported strange phenomena associated with microwave processing that cannot be explained easily by the differences between conventional and microwave heating, such as increases in reaction rates and yield, decreases in temperature for reactions and differences in reaction pathways and products. The exact mechanism of microwave heating or interactions of microwave with materials still cannot be explained effectively by existing theories, because of the complexities in the interactions involved between different types of materials and microwaves.

1.5 Biomolecule-assisted synthesis, L-cysteine

Due to environmentally concerns, a biomolecule-assisted synthesis, an environment-friendly method, has been developed to produce several nanomaterials. It is known that biomolecules, as life's basic building blocks, have special structures and fascinating self-assembling functions, which make them templates for the design and synthesis of complicated structures [58]. For instance, CdTe branched wires have been successfully synthesized by using amphiphilic biomolecules as templates. Glutathione (GSH) as both assembling molecules and the sulfur source has been use to synthesize snowflake-like bismuth sulfide nanorods under microwave irradiation. Starch has also been introduced to be the reducing and morphology-directing agent for the preparation of tellurium nanowires [59].

L-cysteine is a thiol-containing amino acid which has been extensively used in pharmaceutical, foodstuff, cosmetic, chemical synthesis and using L-cysteine as the sulfur source for metal sulfide synthesis [60-61]. Many researchers have applied L-cysteine in a biomolecule-assisted synthesis of binary- and ternary- metal sulfide

compounds in order to produce different micro- and nano- materials with remarkable morphologies, such as PbS nanocube-based pagoda-like hierarchical architectures [59], 3D Fe_3S_4 flower-like microspheres [62], MoS_2 microspheres with nanorods [63], Ag_3SbS_3 nanorods [61], etc. Several conventional and novel methods were assisted with utilizing biomolecule which are used as templates, reactants, reducing agents, and complexing agents for synthesis of important materials. For example:

1.5.1 Biomolecule-assisted hydrothermal synthesis

A hydrothermal treatment of $Pb(CH_3COO)_2$ and L-cysteine solution could produce nanocube-based pagoda-like PbS hierarchical a rchitectures which was reported by Fan Zuo group [59]. The biomolecule, L-cysteine, exerts coordination, oriented nucleation of crystals, and the morphology modulating effect. They supposed that the function groups in the cysteine molecule such as $-NH_2$, -COOH, and -SH have a strong tendency to interact with inorganic cations. When mixing the L-cysteine and $Pb(CH_3COO)_2$ solution, Pb^{2+} could interact with cysteine molecules to form precursor complexes. Following process, the coordinate bond between L-cysteine and Pb^{2+} were ruptured when the reaction temperature became higher (120 °C). The reactions taking place in the system can be described as follows:

$$Pb^{2+} + \text{n L-cysteine} \rightarrow [Pb(\text{L-cysteine})_n]^{2+}$$

$$[Pb(\text{L-cysteine})_n]^{2+} \rightarrow PbS$$

When the $Pb(CH_3COO)_2$ solution and L-cysteine solution were mixed for a period of time, a grayish-green suspension was obtained. The suspension, expected to

be the precursor formed by L-cysteine and $Pb(CH_3COO)_2$, had been confirmed by FTIR spectra. The characteristic peaks of amino acids, from the diagnostic vibrations of acylamino (-CO-NH_2-) bonding were observed. The other peaks were the characteristic peaks of the amido (-NH_2), and -SH signal. The XRD pattern also demonstrated that the precursor was composed of the complex of L-cysteine and $Pb(CH_3COO)_2$ rather than PbS.

1.5.2 Biomolecule-assisted solvothermal synthesis

A facile l-cystine assisted approach has been developed to synthesize Ag_3SbS_3 nanocrystalline under solvothermal conditions, in which l-cystine is used as the sulfide source and complexing agent [61]. No nauseous scent (H_2S) appears in the experiments. The formation mechanism for Ag_3SbS_3 nanocrystalline is presented. The preparation of solution of $AgNO_3$–(l-cystine) and $SbCl_3$–(l-cystine) is a key factor to form Ag_3SbS_3 phase. First, Ag^+ and Sb^{3+} can complex with l-cystine molecules to form $[Ag(\text{l-cystine})_n]^+$ and $[Sb(\text{l-cystine})_n]^{3+}$ complexes in the solution, respectively. The process will not produce large number of free dissociative S^{2-}, Ag^+, and Sb^{3+}, this can prevent Ag_2S or Sb_2S_3 formation in the solution. Second, at a suitable temperature, the $[Ag(\text{l-cystine})n]^+$ and $[Sb(\text{l-cystine})n]^{3+}$ undergo thermal decomposition to produce Ag_3SbS_3 nanorods. At this stage, due to the relative stability of the complexes, decomposition will proceed more slowly and produce a smaller number of nuclei in the solution than the direct ion-exchange reaction.

1.5.3 Biomolecule-assisted microwave radiation synthesis

In this research, we report a different approach for the synthesis of Cu_3BiS_3 dendrite, utilizing cyclic microwave radiation (CMR) using a genetically coded amino acid (L-cysteine). No one has ever succeeded in synthesizing Cu_3BiS_3 dendrites by this process. These products are also crystalline and phase-pure.

1.5.4 L-Cysteine

Cysteine (symbol as Cys or C) is an α-amino acid with the chemical formula $HO_2CCH(NH_2)CH_2SH$. It is a non-essential amino acid, which means that it is biosynthesized in humans. Its codons are UGU and UGC. Cysteine is a precursor of methionine and also thiamine, biotin, lipoic acid, coenzyme A and coenzyme M. Cysteine also plays an important role in the biogenesis of [Fe – S] clusters, is found in the catalytic site of several enzymes and aids protein folding and assembly by forming disulfide bonds. As a result of its crucial role in cellular physiology and the reactivity of the -SH group, cysteine metabolism is tightly controlled in response to environmental variations. Cysteine is also biotechnologically interesting as a nutritional supplement, a pharmaceutical (antidote) or a precursor for drugs [64].

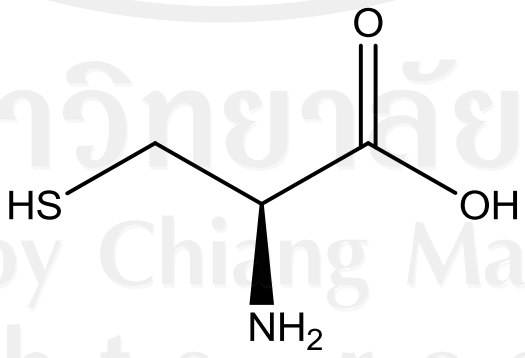

Figure 1.7 Molecular structure of L-cystiene

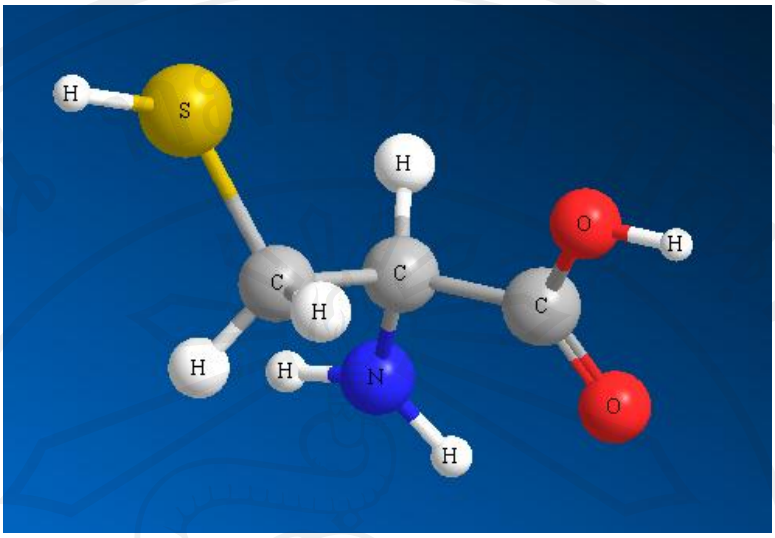

Figure 1.8 Simulated molecular structure of L-cystiene

In microorganisms, sulfur from sulfate, thiosulfate or sulfonates as sole sulfur sources is necessary for the synthesis of cysteine. These compounds are taken up by specific transporters followed by the conversion of sulfate or sulfonates into sulfide in 2 to 4 steps. The biosynthesis of cysteine from serine in bacteria is carried out by a two-step pathway. Some microorganisms can also use methionine or cysteine-derived compounds such as glutathione as sole sulfur source. The thiol group of the amino acid cysteine is readily deprotonated under physiological conditions, and the resulting thiolate is one of the most reactive functional groups found in proteins. Studying of static distribution of cysteine residues in protein of known structure, it is surprisingly that cysteine residues played strongly hydrophobicity [65]. Moreover, the research results imply that free cysteines behave as strongly hydrophobic, and not hydrophilic, residues in proteins.

Biomolecules with many functional groups can coordinate with metal cations and form metal–biomolecule complexes, which can serve as precursors of inorganic

nanomaterials. In the l-cystine molecule, there are many functional groups, such as –NH_2, –COOH, and –SH, which have a strong tendency to coordinate with inorganic cations and to form high-affinity metal–biomolecule complexes.

1.6 General characterization techniques for ternary metal sulfide materials

In this past, the microstructural characterizations are presented to assess physical and chemical properties of synthesized samples. The crystallographic phases of samples, the morphology of these phases and also the local chemical composition are determined by XRD, EDX, SEM, TEM, SAED, and HR-TEM techniques. Following, the optical properties of sample were studied.

1.6.1 Structural characterization

1.6.1.1. X-ray diffraction (XRD)

X-ray technology has more than a hundred years of history and the discovery and development of X-ray has revolutionized many areas of modern science and technology. The phenomenon of X-ray diffraction (XRD) by crystals was discovered in 1912 by Max von Laue. The Bragg's law, which is diffraction condition in a simple mathematical form, was also formulated by Lawrence Bragg in the same year [66]. At present, X-ray diffraction is a tool that is useful for the determination of structural data at a very high level of precision [67]. The atomic level structure of the material can be determined by analyzing the diffraction pattern. The technique allows for the unambiguous determination of the positions of the atoms and ions that make up a molecular or ionic compound and thus allows description of structures in terms of features such as bond lengths and angles.

Diffraction is the interference between waves that occurs as a result of an object in their path. XRD techniques are based on elastic scattered X-rays from matter by electron in atoms. Due to the wave nature of X-rays, the scattered X-rays from a sample can interfere with each other such that the intensity distribution is determined by the wavelength and the incident angle of the X-rays. The expression of the space distribution of the scattered X-rays is referred to as an X-ray diffraction pattern. According to the Bragg's law, diffraction from a crystalline sample can be explained and visualized by using a simple notion of mirror reflection of the incident X-ray beam from a series of crystallographic planes [68]. Bragg's law forms the foundation for x-ray diffraction is as below.

$$n\lambda = 2d \sin \theta$$

This equation verifies certain relationships among the diffraction angle (Bragg angle, θ), wavelength of X-ray (λ), and interplanar spacing of crystallographic planes (d).

There are several X-ray diffraction techniques utilized in many researches. Single crystal X-ray diffraction (SCD) is a technique used to solve the complete structure of crystalline materials, typically in the form of single crystals. X-ray powder diffraction (XRPD), got its name from the technique of collecting X-ray diffraction patterns from packed powder samples. Generally, X-ray powder diffraction involves the characterization of the crystallographic structure, crystallite size, and orientation distribution in polycrystalline samples. A small-angle X-ray scattering (SAXS) technique is used for measuring the scattering intensity at scattering angles within a few degrees from the incident angle. SAXS pattern reveals

the material structures, particle size and shape, in the nanometer to micrometer range. In contrast to SAXS, wide-angle X-ray scattering (WAXS) is also another X-ray diffraction technique. By definition, X-ray diffraction (XRD) covers SCD and XPRD as well as many X-ray diffraction techniques.

For the X-ray powder diffraction, the materials being studied are in polycrystalline form, a powder sample contains an enormous number of very small crystallites, typically 0.1-10 μm in dimension and orientated at random. An X-ray striking a polycrystalline sample is scattered in all possible direction. As a result, each plane of atoms separated by different lattice spacing in the crystal gives rise to a cone of diffraction intensity. The scattered intensity diffracted by a polycrystalline sample is measured as a function of Bragg angle, 2θ. Hence, powder diffraction patterns (figure1.9) are usually plotted in the form of the measured intensity (total number of the accumulated counts, counting rate (counts per second – cps) or in arbitrary units) versus the Bragg angle. A diffraction pattern may be analyzed at two levels. A crystalline material may be identified from its diffraction pattern by comparing the diffraction angles that correspond to the peaks in the spectrum and their relative intensities with a diffraction standard (for example, the JCPDS file). In this procedure the diffraction spectrum is treated as a fingerprint of the crystal structure in order to identify the crystalline phases. Alternatively, the diffraction spectrum may be compared with a calculated spectrum, derived from some hypothetical model of the crystal structure. The extent to which the predicted spectrum fits the measured data, the degree of fit, then determines the confidence with which the model chosen is judged to represent the crystal structure [69].

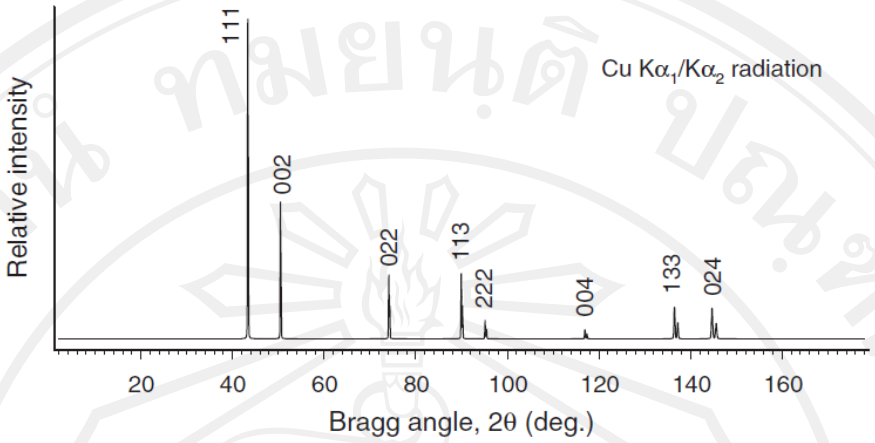

Figure1.9 The simulated powder diffraction pattern of copper (space group $Fm\bar{3}m$, a = 3.615 Å, Cu $K_{\alpha1}/K_{\alpha2}$ radiation, Cu atom in 4(a) position with x = 0, y = 0, z = 0). (after Ref. 68)

Table 1.1 Powder diffraction pattern as a function of various crystal structure, specimen and instrumental parameters (after Ref. 68)

Pattern component	Crystal structure	Specimen property	Instrumental parameter
Peak position	**Unit cell parameters:** $(a, b, c, \alpha, \beta, \gamma)$	*Absorption*	**Radiation (wavelength)**
		Porosity	*Instrument/sample alignment*
			Axial divergence of the beam
		Preferred orientation	
Peak intensity	**Atomic parameters** $(x, y, z, B,$ etc.)	Absorption	Geometry and configuration
		Porosity	**Radiation (Lorentz, polarization)**
	Crystallinity	*Grain size*	**Radiation (spectral purity)**
Peak shape	Disorder	*Strain*	**Geometry**
	Defects	*Stress*	**Beam conditioning**

[a] Key parameters are shown in **bold**. Parameters that may have a significant influence are shown in *italic*.

Typical powder diffraction pattern may contain the following components: positions, intensities, and shapes of multiple Bragg reflections. Each of the three components represents information about the crystal structure of the material, the properties of the specimen (sample), and the instrumental parameters as in Table 1.1.

1.6.1.2 Scanning electron microscopy (SEM)

The scanning electron microscope is a versatile instrument available for the examination and analysis of the microstructure morphology and chemical composition characterizations [70]. SEM technique provides the scientist with images that closely approximate what the physiology of the eye and brain expect, since the depth of field for resolved detail in SEM is very much greater than the spatial resolution in the field of view of human [69].

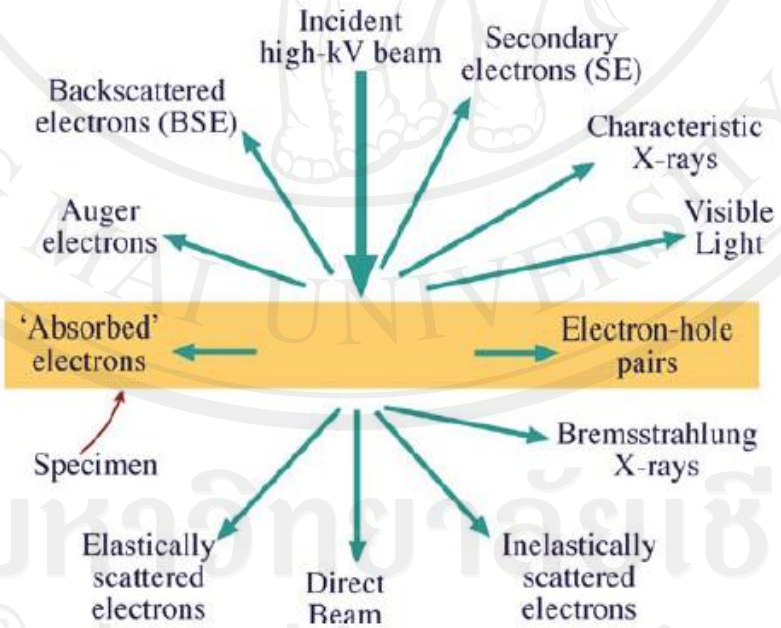

Figure 1.10 Signals generated when a high-energy beam of electrons interacts with a thin specimen. [after Ref. 71]

SEM image is derived from the acquisition of signals produced from the electron beam and specimen interactions. These interactions can be divided into two major categories: inelastic scattering and elastic scattering. The most commonly used signal is that derived from low energy secondary electrons (SE), which are ejected from the surface of the target by the inelastic scattering of electron beam with the sample. The primary electron beam loses energy by transferring substantial energy to that target atom as the electron penetrates beneath the sample surface. Another signal is also come from backscattered electrons (BSE), which is the incident electrons that are elastically scattered through an angle of more than 90° degree. This electron is characterized by negligible energy loss during the collision and by a wide-angle directional change after scattering. In addition to those signals that are utilized to form an image, a number of other signals are produced when an electron beam strikes a sample (Figure 1.10), including characteristic X-rays, generated by excitation of inner shell electrons; cathodoluminescence, excitation in the range of visible light that is associated with valency electron excitation; and specimen current passing through the sample due to the net absorption of electric charge.

The main components of the scanning microscope (Figure 1.11) include the microscope column, the various signal detector systems, the computer hardware and software used to process the collected data, and the display and recording systems. The microscope column is kept under vacuum, and the vacuum system and specimen air-lock are an integral part of the microscope system. The electron source or electron gun can be a tungsten filament, or a LaB_6 or Schottky emitter, or a tungsten field-emission tip. The incident electron beam (also know as the electron probe) needs to be as small as possible (1-10 nm) and the electron probe is scanned horizontally across

the specimen in two perpendicular (x and y) directions. By scanning simultaneously in two perpendicular directions, a square or rectangular area of specimen (known as a raster) can be covered. The electromagnetic probe lens is used to focus the electron beam onto the specimen surface in SEM. The best resolution obtainable cannot be better than the incident-probe diameter on the sample surface. An image of the surface area can be formed by collecting secondary electron from each point on the specimen. The same raster-scan signals can be used to deflect the beam generated within a cathode-ray-tube (CRT), in exact synchronism with the motion of the electron beam that is focused on the specimen. If the SE signal is amplified and applied to the electron gun of the CRT (to change the number of electrons reaching the CRT screen, the resulting brightness variation on the phosphor represents a SE image of the specimen. In raster scanning, the image is generated serially (point by point) rather than simultaneously. A similar principle is used in the production and reception of television signals.

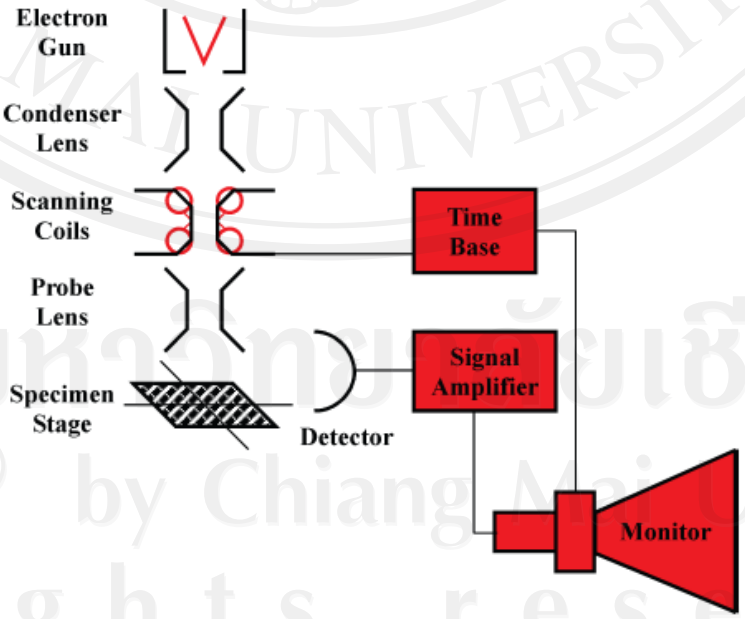

Figure 1.11 The Schematic diagram of scanning electron microscopy (after Ref. 72)

One major advantage of the SEM (in comparison to a TEM) is the ease on specimen preparation. In fact, many conducting specimens require no special preparation before examination in the SEM. On the other hand, specimen of insulating materials do not provide a path to ground for the specimen current (I) and many undergo electrostatic charging when exposed to the electron probe [72]. The local charge on the specimen can be positive or negative. Negative charge presents a more serious problem, as it repels the incident electrons and deflects the scanning probe, resulting in image distortion or fluctuations in image intensity. The solution to the charging problem is coating the surface of specimen with thin film of metal or conducting carbon by the evaporation or sublimation technique in vacuum system. The film of thickness 10-20 nm conducts sufficiently to prevent charging of most specimens because this thickness is greater than the secondary electron escape depth, the secondary electron comes from the coating rather than from the specimen material. Gold and carbon are common coating materials. For evaporated carbon, it has a low secondary electron yield but an extremely small grain size so that we will not see the granularity of the coating in a high-magnification SEM image. Where coating is undesirable or difficult for example the rough surface, specimen charging can be avoided by carefully choosing the SEM accelerating voltage. The use of low-voltage SEM is therefore a practical option for imaging insulating specimens.

1.6.1.3 Transmission electron microscopy (TEM)

The electron microscope extends the resolution available for morphological studies from that dictated by the wavelength of visible light to dimensions which are well into the range required to image the lattice planes in a crystal structure, which is from of the order of 0.3 mm to of the order of 0.1 nm. The TEM is capable of displaying magnified images of a thin specimen, typically with a magnification in the

range 10^3-10^6. The most important characteristic of the TEM is that it combines information from objects in real space at excellent resolution, sub-nanometer and even sub-Å angstrom resolution, with information from the same object obtained in reciprocal space, that is, electron diffraction patterns can be recorded. Assembling with other microanalytical techniques that can be integrated into the same instrument makes TEM one of the most versatile and powerful tools available for microstructural characterization. For instance, selected-area electron diffraction (SAED) is an indispensable part of TEM and is arguably the most useful aspect for investigation of crystal structure (and particularly crystal defects) [71].

TEM operates in an analogous way to a transmission optical microscope, but TEM microscope is usually 'upside down', by the source of the electron beam is at the top of the microscope while the recording system is at the bottom. An electron gun replaces the optical light source and is maintained at a high voltage with respect to earth (typically 100–400 kV). The high energy electrons from the gun are focused by an electromagnetic condenser lens system. Focusing of the image in the TEM is not obtained by adjusting the position of the specimen along the z axis to alter its distance from the objective lens, but rather by changing the lens current in order to adjust the focal length of the electromagnetic lens for focusing a first image from the elastic scattered electrons that have been transmitted through the thin film specimen. The final imaging system also employs electromagnetic lenses, and the final image is observed on a fluorescent screen that converts the high energy electron image into an image that is visible to the eye. The development of charge-coupled devices (CCDs) combined with computerized image processing can be used for making digital image recording outcomes. A simplified TEM setup is shown in Figure 1.12. The high

energy electron beam has a limited path length in air, so that the whole electron microscope column must be kept under vacuum. In general, the vacuum needs to be better than 10^{-6} Torr, while for the highest resolution a vacuum of 10^{-7} Torr is desirable.

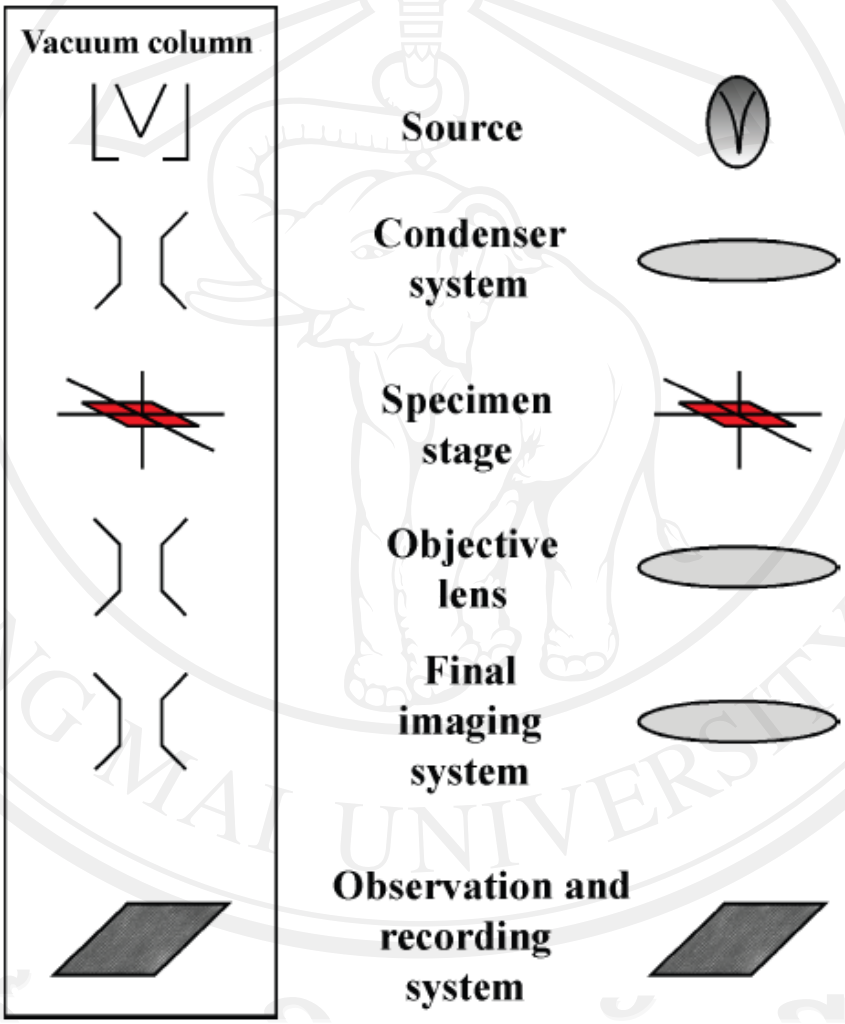

Figure 1.12 Schematic diagram of a TEM set-up (after Ref. 69)

Samples for conventional TEM commonly need to be thinned uniformly to less than 100 nm because electrons must be transmitted through the material. While those for lattice imaging in high resolution TEM (HR-TEM) or sub-micrometre microanalysis by electron energy loss spectroscopy (EELS) should be less than 20 nm thick. The electron beam interacts with a thin-film specimen both elastically and inelastically, but it is the elastic interactions that dominate the contrast observed in the microscope. Contrast arises from three quite distinct image-forming processes, and these are termed mass–thickness contrast, diffraction contrast and phase contrast, respectively. In crystalline specimens, the use of the primary beam (bright field) or a Bragg-reflected beam on-axis (dark field) gives rise to diffraction contrast, which is important for the imaging of crystal defects. When Bragg-diffracted beams also pass through the aperture, crystal-structure imaging reveals projections of atomic rows. On the other hand, the inelastic interaction contains information on the chemical composition of the sample, in EELS technique.

1.6.1.4 Selected area electron diffraction (SAED) [73]

Since the wavelength of an accelerated electron in a TEM is much smaller than an X-ray beam, the Ewald sphere (radius: $1/\lambda$) is significantly larger for electron diffraction relative to X-ray diffraction studies. As a result, electron diffraction yields much more detailed structural information of the crystal lattice. Information such as lattice parameters and atomic positions in a crystal may be obtained through analyzing electron diffraction pattern. This technique is well known as selected area electron diffraction pattern (SAED). In addition, the lenses within a TEM can be altered the orientation of the incoming electron beam from a parallel beam to a cone-shape beam. The later orientation is known as convergent beam electron diffraction (CBED), and

the lenses within a TEM allows one to contact a diffraction experiment over many incident angles simultaneously to reveal the full three-dimensional reciprocal lattice of the crystal.

By examining the systematic absences of the diffraction spot (Table 1.2), electron diffraction pattern may determine the appropriate Bravais lattice as well as any screw axes and glide planes that are present in the crystal lattice. By comparison with X-ray diffraction, TEM/SAED is the best alternative to investigate the structural information from an individual nanocrystal but the structural information from a bulk crystalline solid should come from X-ray diffraction.

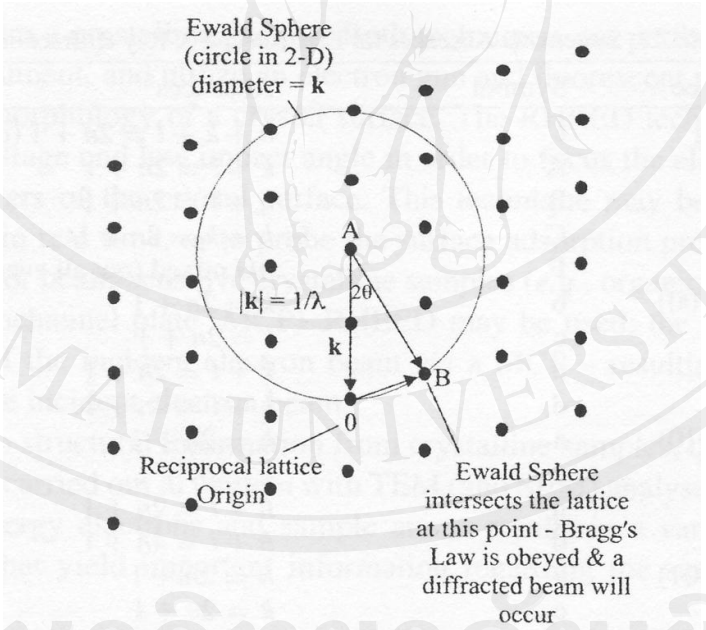

Figure 1.13 Illustration of Ewald sphere construction, and diffraction from reciprocal lattice point (after Ref. 73)

Table 1.2 Systematic Absences for Electron and X-ray diffraction (after Ref. 73)

Cause of absence	**Symbol**	**Absences**
Body-centering	I	h+k+l = 2n + 1 (odd)
A centering	A	k+l = 2n+1
B centering	B	h+l = 2n+1
C centering	C	h+k = 2n+1
Face-centering	F	hkl mixed (not all even or all odd)
Glide plane//(100)	b	k = 2n+1
	c	l = 2n+1
	n	k+l = 2n+1
	d	k+l = 4n+1
Glide plane//(010)	a	h = 2n+1
	c	l = 2n+1
	n	h+l = 2n+1
	d	h+l = 4n+1
Glide plane//(001)	a	h = 2n+1
	c	k = 2n+1
	n	h+k = 2n+1
	d	h+k = 4n+1
Screw axis//a	2_1 or 4_2	h = 2n+1
	4_1 or 4_3	h = 4n+1
Screw axis//b	2_1 or 4_2	k = 2n+1
	4_1 or 4_3	k = 4n+1

Table 1.2 (Continued) Systematic Absences for Electron and X-ray diffraction (after Ref. 73)

Screw axis//c	2_1 or 4_2	l = 2n+1
	3_1, 3_2, 6_2, or 6_4	l = 3n+1, l = 3n+2
	4_1 or 4_3	l = 4n+1, 4n+2, 4n+3
	6_1, or 6_5	l = 6n+1, …., 6n+5
Screw axis//(110)	2_1	h = 2n+1

The absence refers to the Miller indices (hkl values) that are absent from the diffraction pattern. For example, a body-centered cubic lattice with no other screw axes and glide planes will have a nonzero intensity for all reflections where the sum of (h+k+l) yields an odd number, such as (100), (111), etc. Other reflections from planes in which the sum of their Miller indices are even, such as (110), (200), will be present in the diffraction pattern.

1.6.1.5 Raman spectroscopy (Raman) [74]

Raman spectroscopy is regarded as one technique of the vibrational spectroscopy which provides characteristic fundamental vibrations that are employed for the illustration of molecular structure. Raman spectroscopy involves the study of the interaction of radiation with molecular vibrations which photon energy is transferred to the molecule by changing its vibrational state. Although some vibrations may be active in both Raman and IR spectroscopy, these two forms of spectroscopy arise from different processes and different selection rules. Raman spectroscopy is best at symmetric vibrations of non-polar groups while IR spectroscopy is best at the asymmetric vibrations of polar groups.

Raman spectroscopy composes of a two-photon inelastic light-scattering event which known as “Stokes or Anti-stokes Raman scattering”. Light scattering phenomena may be classically described in terms of electromagnetic (EM) radiation produced by oscillating dipoles induced in the molecule by the EM fields of the incident radiation. The light scattered photons include mostly the dominant Rayleigh and the very small amount of Raman scattered light. The induced dipole moment occurs as a result of the molecular polarizability α, where the polarizability is the deformability of the electron cloud in the molecule by an external electric field.

The incident electromagnetic field (E) will perturb the charged particles of the molecule resulting in an induced dipole moment (μ).

$$\mu = \alpha E$$

In order for Raman bands to be observed, the molecular vibration must cause a change in the polarizability.

In a typical Raman experiment, a laser is used to irradiate the sample with monochromatic radiation. Laser sources are available for excitation in the UV, visible, and near-IR spectral region (785 and 1064 nm). The Raman vibrational bands are characterized by their frequency (energy), intensity (polar character or polarizability), and band shape (environment of bonds). Since the vibrational energy levels are unique to each molecule, the Raman spectrum provides a “fingerprint” of a particular molecule. The frequencies of these molecular vibrations depend on the masses of the atoms, their geometric arrangement, and the strength of their chemical bonds. The spectra provide information on molecular structure, dynamics, and environment.

The Rayleigh and Raman processes are depicted in Figure 1.14. No energy is lost for the elastically scattered Rayleigh light while the Raman scattered photons lose

some energy relative to the exciting energy to the specific vibrational coordinates of the sample. The laser excitation frequency (ν_L) is represented by the upward arrows and is much higher in energy than the molecular vibrations. The frequency of the scattered photon (downward arrows) is unchanged in Rayleigh scattering but is of either lower or higher frequency in Raman scattering. The dashed lines indicate the "virtual state." Both Rayleigh and Raman are two photon processes involving scattering of incident light, from a "virtual state." The incident photon is momentarily absorbed by a transition from the ground state into a virtual state and a new photon is created and scattered by a transition from this virtual state. Rayleigh scattering is the most probable event and this scattered photon results from a transition from the virtual state back to the ground state and is an elastic scattering of a photon resulting in no change in energy. Raman scattering is far less probable than Rayleigh scattering and this scattered photon results from a transition from the virtual state to the first excited state of the molecular vibration. This is described as an inelastic collision between photon and molecule, since the molecule acquires different vibrational energy (ν_m) and the scattered photon now has different energy and frequency.

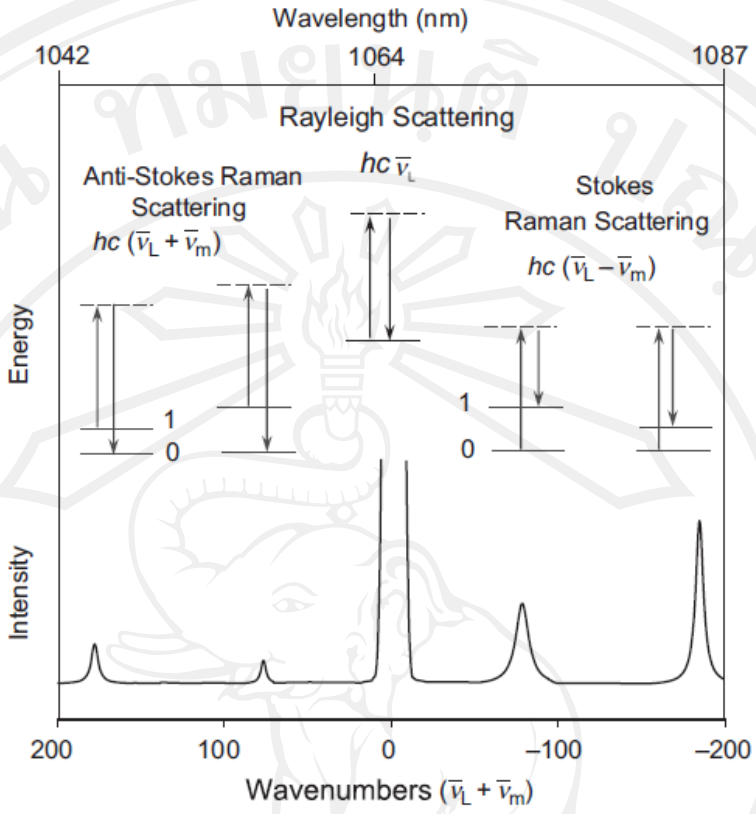

Figure 1.14 Schematic illustrations of Rayleigh scattering as well as Stokes and anti-Stokes Raman scattering. (after Ref. 74)

1.6.1.6 X-ray Photoelectron spectroscopy [73]

The photoelectric effect is first outlined by Einstein in the early 1900s; refer to the ejection of electrons from a surface due to photon impingement. Until the 1960s, photoelectric phenomenon was exploited for surface analysis technique as X-ray photoelectron spectroscopy (XPS). This technique consists of the irradiation of a sample with monochromatic X-ray, which releases photoelectron from the sample surface (Figure 1.15). Due to the short free mean path of the photoelectron in solid, this technique provides compositional information from only the top 1-5 nm of a sample. Each of atoms in the sample has characteristic binding energies of their inner-

shell electrons, referred to as absorption edge. In order to excite the electrons, the energy of the incident photons (hν) must be at least as large as the binding energy (E_b) of the electrons. When this energy threshold is exceeded, a large absorption of energy takes place, followed by the release of photoelectrons with excess kinetic energy (E_k) as in Equation below in order to relax the atom back to its stable ground state.

$$E_k = h\nu - E_b$$

Where E_k = kinetic energy of the emitted photoelectron, hν = the energy of the incident photon, and E_b = the binding energy of the inner-shell electrons.

Since the binding energy of an atom is already by minute changes in its chemical environment, (such as oxidation state, hybridization, etc), XPS provides both elemental quantification and details regarding the chemical environment of the surface atom.

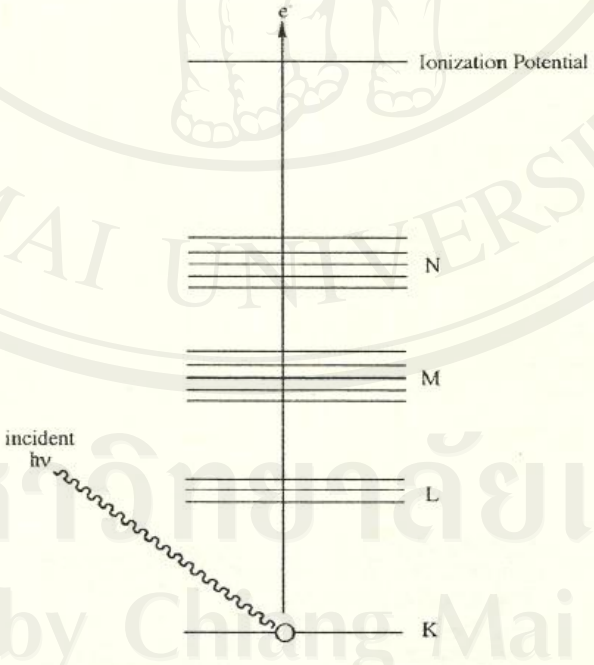

Figure 1.15 The energy-level diagram for X-ray photoelectron spectroscopy (XPS) (after Ref. 73)

1.6.2 Optical characterization

This part is the studying of optical phenomena in ternary metal sulfide compounds. These optical processes involve absorption and emission of electromagnetic radiation from the sample. The absorption and emission are related to each other. In absorption process, energy is removed from an incident electromagnetic wave while microscopic entities (i.e., elementary particles, ions, atoms, or molecules) are excited to a higher energy level (excited or final state). Emission process is the inverse, microscopic entities decay from a high-energy excited state to lower energy level (ground or fundamental state).

Absorption spectra provide rich information on the energy levels of the material, such as inner or valence electrons, vibrations or rotations of molecules or defects in condensed matters, a variety of energy gaps and elementary excitations, e.g. phonons and excitons.

1.6.2.1 UV-Vis- NIR spectroscopy [75-77]

UV-Vis-NIR spectroscopy is widely utilized to characterize organic molecules and inorganic nanostructure. A sample is irradiated with electromagnetic waves in the ultraviolet, visible and near IR ranges and the absorbed light is analyzed through the resulting spectrum. The samples can be either organic or inorganic, and may exist in gaseous, liquid or solid form. Herein, the used of this technique for characterizing inorganic nanomaterials will be mentioned. Size dependant properties can be observed in the spectrum, particularly in the nano and atomic scales. These include peak broadening and shifts in the absorption wavelength. Many electronic properties, such as the band gap of a material, can also be determined by this technique. The energies associated with UV-NIR ranges are sufficient to excite electrons from

valance band (HOMO) to conduction band (LUMO). Photons in the visible range have wavelengths between 800-400 nm, which corresponds to energies between 1.55 and 3.10 eV. The near UV range includes wavelengths down to 200 nm, and has energies as high as 6.20 eV. The near IR region covers wavelengths between 800-1500 nm (1.55-0.83 eV). As a result, UV-Vis-NIR spectroscopy is an ideal technique for determining the electronic properties of both large and narrow band gap nanomaterials. In the spectrum of nanoparticles, the absorption peak's width strongly depends on the particle sizes and shapes. As a result, their spectrum is different from their bulk counterparts. For instance, for semiconductor nanocrystals, the absorption spectrum is broadened owing to quantum confinement effects and as their size reduces. Furthermore, semiconductor nanoparticles's absorption peaks shift towards smaller wavelengths (higher energies) as their crystal size decreases. An important consequence of using this technique is that the band gap of nanosized materials can be determined. For semiconductors, a classical Tauc approach was employed to estimate their optical energy band gaps using the following equation:

$$\alpha h\nu = A(h\nu - E_g^{opt})^{m/2},$$

where A is a constant, α is the absorption coefficient ,and m equals 1 or ½ for a direct transition and indirect band gap, respectively. h is the Planck constant, ν is the frequency, and E_g^{opt} is the optical band gap. A plot of $(\alpha h\nu)^2$ against $(h\nu)$ for a direct transition. The value of $(\alpha h\nu)^2$ extrapolated to $\alpha = 0$ gives an optical band gap

The consequence of E_g is that we can use it to investigate the position of valance band energy, which is an important data for photocatalytic application, by using the following equation:

$$E_{VB} = X - E^e + 0.5E_g$$

where E_{VB} is the valance band edge potential, X is the electronegativity of the semiconductor which is the geometric mean of the electronegativity of the constituent atoms, E^e is the energy of free electrons on the hydrogen scale (≈4.5 eV), and E_g is the band gap energy of the semiconductor.

1.6.2.2 Photoluminescence spectroscopy (PL) [78-80]

Materials emit light by spontaneous emission when electrons in the excited states drop to a lower level. The emitted light is called luminescence.

Luminescence is categorized as follows

1. Photoluminescence (PL) is the re-emission of light after absorbing an excitation light.
2. Electroluminescence (EL) is the emission of light caused by an electric current flowing through the material. This is utilized in optoelectronic devices: the light emitting diode (LED) and the laser diode (LD).
3. Cathodoluminescence (CL) is the emission of light due to irradiation by an electron beam.
4. Chemiluminescence is the emission of light caused by a chemical reaction. Bioluminescence which originates in an organism belongs to chemiluminescence.

The emission of PL radiation is caused by the transition of electrons from higher occupied electronic states into lower unoccupied states, under the emission of photons if the transition is dipole-allowed.

A schematic of a typical PL setup is shown in Figure 1.16. The sample can be mounted in ambient conditions for fast room-temperature measurements or in a

cryostat for low-temperature measurements in vacuum. For excitation source, any light source of suitable luminance and appropriate wavelength range can be used. The most general light source would be a halogen or xenon lamp filtered by a monochromator, which allows for a wide range of excitation wavelengths. In most setups laser excitation sources are used because of the widespread availability and high monochromatic power.

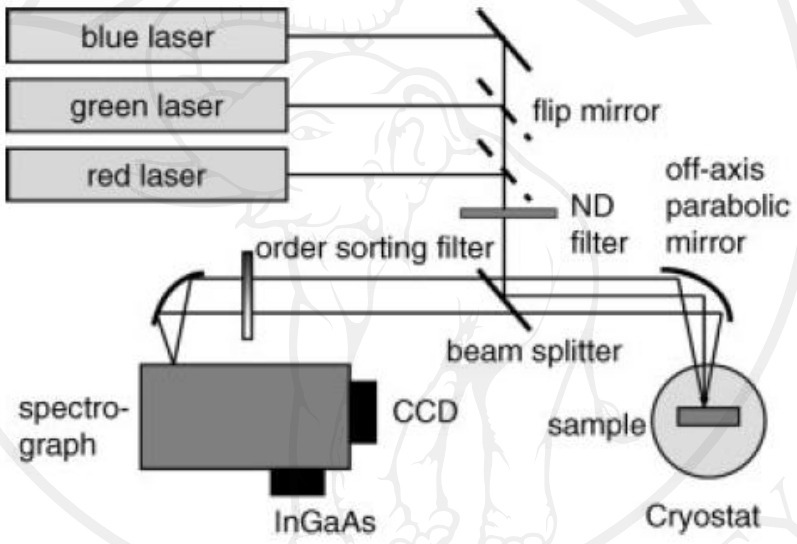

Figure 1.16 Schematic of experimental setup for room- and low-temperature PL measurements (after Ref 79).

The excitation source is focused onto the sample by a flat mirror or focusing device (lens or parabolic mirror). The luminescence radiation emitted from the sample is then collected by a lens or also by a parabolic or off-axis parabolic mirror. The luminescence light is then focused into the monochromator system through an entrance slit. The luminescence light exits the monochromator through an exit slit and reaching the radiation detector, which can be a photodiode, photomultiplier, or a photodiode array or CCD array.

A number of different transitions can occur in a PL measurement depending on the measurement conditions and the material properties. In the following, a very brief description of the most important radiative transitions occurring in semiconductor materials is given. In general, the different transitions can be distinguished by their transition energy and by the change of the transition energy and luminescence yield with varying excitation intensity and temperature. Therefore, it is useful to define the following two dependencies. The luminescence yield of a transition line in general is found to obey the expression

$$Y_{PL}(\phi) = \phi^{k}$$

where ϕ is the excitation intensity and k is a characteristic parameter usually ranging between 0.5 and 2. The luminescence yield of transitions involving localized states generally decreases with increasing temperature owing to the thermal emission of the trapped carriers to the conduction or valence band. This dependence on temperature can be described by

$$Y_{PL}(T) = \frac{1}{1 + C_{exp}(-E_a/kT)}$$

where E_a represents a characteristic activation energy and C is a constant which is proportional to $T^{3/2}$ if the thermal quenching involves thermal emission to the conduction or valence band. Bear in mind that the activation energies can differ significantly if or if not a $T^{3/2}$ dependence is included in the model. The shift of transition energy with increasing temperature may be influenced by a shift in the optical gap with temperature. Typically, a decrease in the band gap with increasing temperature of the order of 10^{-4} eV/K is observed that may compensate positive peak shifts of the order of k_BT in the experiment. Radiative transitions can occur with or

without the emission of phonons, depending on the electron–phonon coupling strength and the measurement temperature, thereby often leading to so-called phonon replica of the transitions.

The classical PL experiment is performed at low temperatures in the vicinity of 10 K. At this temperature, the luminescence efficiency can be considerably higher than that at room temperature as the ratio of radiative to nonradiative recombination rate is greatly increased. The recombination events arising from electron–hole pairs bound to each other by their Coulomb interaction, so-called free excitons, may be observable. The transition energy of free excitons can be calculated using a simple hydrogenic model yielding

$$E_{FX} = E_g - E_x, \qquad E_x = \frac{m_r e^4}{2(4\pi(_0\varepsilon_r \bar{h})^2 n^2}$$

where E_x is the exciton binding energy and m_r is the reduced electron–hole mass $1/m_r^* = 1/m_e^* + 1/m_p^*$. The quantum number n specifies the possible excited states of the exciton. The binding energy of excitons mostly depends on the dielectric constant ε_r and the reduced effective mass.

1.7 Research objectives

1. To synthesize and characterize the chemical, physical and optical properties of ternary metal sulfide, for example Cu_3BiS_3, Cu_3SbS_4 and $CuFeS_2$ nanostructures
2. To investigate the parameters which influence on the preparation of ternary metal sulfide by microwave radiation synthesis.
3. To develop the microwave assisted synthesis method by using cyclic microwave radiation (CMR) which is offer several advantages over other conventional heating techniques.
4. To study the mechanisms of the formations of ternary metal sulfide single phase.